

GPPS-TC-2024-0081

ENTROPY GENERATION RATE OPTIMISATION FOR PROFILED ENDWALL DESIGN FOR AXIAL TURBINES

Pedro A. Martinez-Castro
Durham University

pedro.martinez-castro@outlook.com
Durham, United Kingdom

Richard J. Williams
Durham University

r.j.williams5@durham.ac.uk
Durham, United Kingdom

Grant L. Ingram
Durham University

g.l.ingram@durham.ac.uk
Durham, United Kingdom

ABSTRACT

This paper investigates the formulation of the optimal objective function for aerodynamic design of turbomachinery using genetic algorithms (GA) supported by Computational Fluid Dynamics (CFD). The aim is to outline entropy generation rate minimisation as the most suitable objective function for improving turbomachinery. To this end, the calculation of this variable in RANS-CFD simulations is explained, followed by a sensitivity analysis to mesh size, turbulence model and calculation method in a turbine passage of a low-speed linear cascade. Entropy generation rate minimisation was then used as the objective function to improve profiled endwall (PEW) design for the same cascade. The results of entropy generation rate per unit surface area of optimised designs were compared with previous studies' endwall designs. This confirmed that the PEWs reduce secondary loss by weakening the pressure side of the horseshoe vortex and its interaction with the suction surface boundary layer. Comparison of loss coefficient CFD results with measurements from the reference cascade with original planar and the optimised PEW showed good agreement between simulations and experiments, demonstrating the proposed design approach's effectiveness. This paper recommends adopting entropy generation rate as the objective function because it yields superior designs and provides deeper insights into loss mechanisms.

INTRODUCTION

Entropy generation due to irreversibilities is a direct measure of loss in adiabatic machines such as turbomachinery. Hence, paraphrasing Sir Frank Whittle, one of the main objectives of aerodynamic and thermal design of turbines should be to minimise entropy generation (Whittle, 1981). However, entropy generation does not provide information on the loss sources, so a targeted design to reduce loss based on entropy generation is impractical. The entropy generation rate, on the other hand, is a measure of the local entropy production that can be used to track losses to its origin. Denton (1993) described entropy generation rate as the rate at which "smoke" is being produced and, when convected downstream, is present as the sum of all the "smoke" (loss) produced upstream. Most of the work done around Profiled Endwall (PEW) design has used variables indirectly related to loss that can be accurately predicted using lower resolution grids in Computational Fluid Dynamics (CFD), such as exit flow angle deviation, Secondary Kinetic Energy (SKE), or a combination of both (Rose, 1994; Bergh et al., 2020). These lead to successful designs, but there are examples in the literature where a reduction in SKE led to an increase in loss (Ingram et al., 2005). There are less abundant studies that used the stagnation pressure loss coefficient as a design variable for PEWs (Liu et al., 2017; Kadhim and Rona, 2018). This is closely related to entropy generation but its prediction using CFD was not reliable until recently because of computing and turbulence model limitations (Denton and Pullan, 2012). There are even fewer studies aimed to directly minimise the entropy generation (Wang et al., 2010; Li et al., 2011). So far, entropy generation rate has mostly been used for qualitative analysis to select optimal design changes (Zlatinov et al., 2011; Grewe et al., 2014; Shahpar et al., 2017). Previous work has seldom addressed how effective entropy generation rate is to produce better designs. In addition, more work is needed to investigate if current CFD can be trusted to calculate entropy generation rate for quantitative analysis. This also raises the question of whether the understanding of the loss reduction mechanisms of PEWs would benefit from a design aimed to minimise entropy generation rate. This paper examines how entropy generation rate can be used to improve the aerodynamics of turbomachinery.

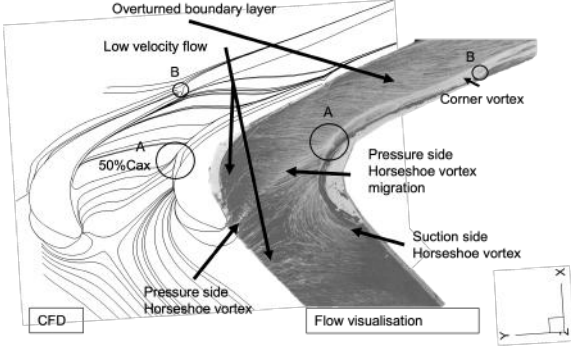


Figure 1 Endwall surface flow pattern ($z = 0$ span): left, CFD predictions; right, flow visualisation from Ingram (2003)

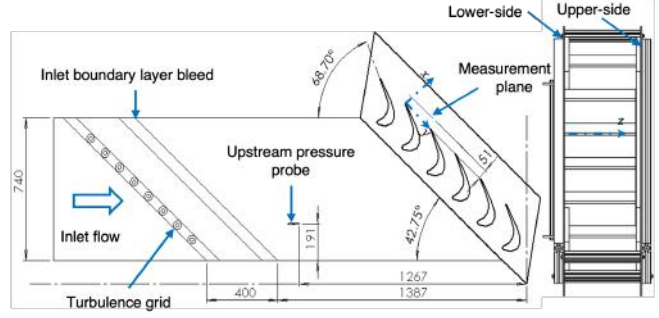


Figure 2 Durham Cascade layout third angle projection including definitions of cascade coordinates and yaw angle.

Secondary flow

The loss associated with secondary flow can represent 1/3 of the total loss in a large hub to tip ratio passages Denton (1993). The entropy generation mechanism has been well studied Sieverding (1985) and originates from the dissipation of the SKE that is induced from the secondary velocities associated to the secondary flow. Figure 1 shows the secondary flow structures. The separation of the inlet boundary layer (BL) due to radial and axial static pressure gradients upstream the blade Leading Edge (LE) gives origin to the Horseshoe Vortex (HV) with two legs: one on the suction side (SSHV) and one on the pressure side (PSHV). The SSHV moves downstream into the passage following the blade's suction surface with an opposite direction of rotation than the PSHV. The PSHV travels downstream across the passage towards the suction side (SS) of the neighbouring blade where it merges with the incoming SSHV to form the passage vortex (PV). A Corner Vortex (CV) is induced due to the interaction of the PV with the blade suction surface at the trailing edge (TE).

The stagnation pressure loss coefficient is a measure of entropy generation defined by Equation (1). Note that in this work the upstream dynamic pressure is used for the definition of stagnation pressure loss.

$$Cp_0 = \frac{P_{0in} - P_0}{0.5\rho U_{in}^2}. \quad (1)$$

Another parameter used widely in the literature as an indirect metric of entropy generation in secondary flows is the Secondary Kinetic Energy Coefficient (C_{ske}):

$$C_{ske} = \frac{(U \sin(\alpha - \alpha_{mid}))^2 + u_z^2}{U_{in}^2}, \quad (2)$$

where α is the yaw angle. The first term of the numerator is the secondary velocity U_{sec} . One should be careful when using C_{ske} as not all is related to secondary loss (Brennan et al., 2001) and the calculation of this parameter depends on the arbitrary definition of U_{sec} . For this paper the definition of Ingram (2003) was used as is based on the Durham Cascade reference frame.

Entropy generation rate per unit volume

From a design point of view, turbomachinery features that cause a high rate of entropy generation in the flow should be identified as loss sources and improved. In order to identify these loss sources, the entropy generation rate can be obtained with the transport equation of entropy production per unit volume due to viscous dissipation of mechanical energy. In a RANS simulation this is obtained from the sum of the time-mean or direct dissipation rate \tilde{S}_{gen}''' plus the fluctuating or turbulent dissipation rate \tilde{S}_{gen}''' . To implement this in a RANS simulation Kock and Herwig (2005) proposed calculating the entropy generation rate per unit volume \tilde{S}_{genH}''' turbulent term as:

$$\tilde{S}_{genH}''' = \beta \frac{\rho \omega k}{T}, \quad (3)$$

where $\beta = 0.09$ is one of the $k - \omega$ model closure constants. By contrast, Grewe et al. (2014) used the turbulent viscosity to calculate the turbulent dissipation:

$$\tilde{S}_{genG}''' = \frac{\mu_t}{T} \frac{\partial \bar{u}_{ij}}{\partial x_{ij}} \quad (4)$$

Table 1 Durham Cascade design parameters

| | |
|----------------------------------------------------|--------|
| Inlet flow angle | 42.75° |
| Blade exit angle | -68.7° |
| Blade axial chord | 181mm |
| Blade pitch | 191mm |
| Blade span | 375mm |
| Turbulence intensity | 5% |
| Reynolds Number (axial chord and exit velocity) | 4e5 |

Table 2 Entropy generation rate regions as a percentage of the total entropy generation rate in the full computational domain

| Million cells | 2.5 | 5 | 11 | 30 |
|---------------|-----|-----|-----|-----|
| Inlet BL | 1% | 1% | 1% | 1% |
| Inlet MF | 0% | 0% | 0% | 0% |
| Passage BL | 20% | 19% | 18% | 18% |
| Passage MF | 33% | 31% | 31% | 30% |
| Outlet BL | 5% | 5% | 5% | 5% |
| Outlet MF | 6% | 8% | 8% | 10% |
| Mixed-Out BL | 29% | 28% | 28% | 26% |
| Mixed-Out MF | 7% | 8% | 9% | 10% |

The entropy generation rate \dot{S}_{gen}''' per unit volume over the control volume CV is the total entropy change in entropy \dot{S}_{gen} :

$$\dot{S}_{gen} = \int_{CV} \dot{S}_{gen}''' dV = \Delta S. \quad (5)$$

In a typical RANS computation the value of \dot{S}_{gen} rarely converges to the value of ΔS over the same control volume. This can be achieved by increasing the grid density because the quadratic dependence on velocity gradients of the \dot{S}_{gen} term magnifies the discretisation error when integrating \dot{S}_{gen}''' computed for each cell over the control volume (Zlatinov et al., 2011). The transition model of the RANS computation also contributes to reduce the combined effect of discretisation errors due to grid density and turbulent viscosity (Przytarski and Wheeler, 2021). For this reason, a small difference between \dot{S}_{gen} and ΔS is an indication of an accurate resolution of the flow field.

METHODOLOGY

The PEW was designed and built for the Durham Cascade which is a low-speed linear cascade at Durham University for testing secondary flow. It consists of an arrangement of six turbine reaction blades modified to maintain a similar Reynolds number to that of Rolls-Royce RB211 engine high-pressure turbine blade but at a low Mach number. Table 1 summarises the Durham Cascade key parameters. The flow field was solved numerically with a second order steady-state 3D RANS simulation using the commercial software ANSYS Fluent version 19.2. The simulation ran on 16 cores (Intel Xeon E5-2650 v2 with 2.6GHz processors) of the Hamilton High Performance Computing Service at Durham University achieving residuals of 1e-6 for continuity and 1e-7 for velocity components and turbulence variables. The O-H structured mesh varied from 2.5, 5, 11 to 30 million cells. The refinement was performed by adding cells in the axial, tangential and radial directions in the passage and inlet and outlet regions keeping $y^+ = 1$ and a growth ratio of 1.03 for the first 28 cells. The Transition SST turbulence model was used to close the RANS equations. The inlet boundary was set as a velocity inlet with an inlet BL profile specified from experimental measurements reported in Ingram (2003). The turbulence kinetic energy k , the specific dissipation rate of specific turbulent kinetic energy ω and the intermittency γ were specified from the freestream values reported in Moore and Gregory-Smith (1996).

To validate the simulation the best PEW design produced in this paper was built for the Durham cascade at the hub and tip side (0 and 1 span) followed by axial plane traverses using a 5-hole probe to measure the pressure and the flow direction. The same measurements were performed on a planar endwall case (P0) for comparison. The results reported in this paper correspond to the 75% and 128% c_x traverses only. The Durham Cascade layout is shown in Figure 2. The upstream total and dynamic reference pressures were measured using a Pitot-Static pressure probe. Data were sampled in an experimental grid of 96 by 161 points in the tangential and radial direction respectively at each node 1 kHz for 10s and averaged. To achieve the same experimental grid, the radial coordinates on both endways were normalised by the local span that corresponds with their tangential position. Before the experimental campaign, the pressure transducers and 5H-probe were calibrated. The effect the primary and secondary instrumentation uncertainties had in the overall measurement of the main experimental variables reported in this paper was assessed using the Kline McKlintock analysis. The experimental uncertainty for Cp_0 and α was ± 0.04 and $\pm 0.6^\circ$ respectively. More details on the experiments are found in Martinez Castro (2022).

Details of the CFD model and validation process

The total entropy generation rate (Equation 5) calculated using the \dot{S}_{genH}''' (Equation 3) and \dot{S}_{genG}''' (Equation 4) methods was compared to the total change of entropy in the system ΔS for the different mesh resolutions. The computational domain were divided into four main zones in the axial direction and two in the radial direction giving a total of eight zones with different average cell volumes (see Figure 4). A comparison of the values of \dot{S}_{genH} and \dot{S}_{genG} with ΔS for the different

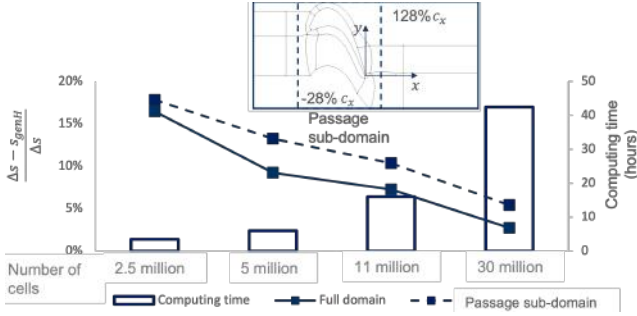


Figure 3 Entropy generation imbalance for the full computational domain and the Passage sub-domain for a Transition SST turbulence model.

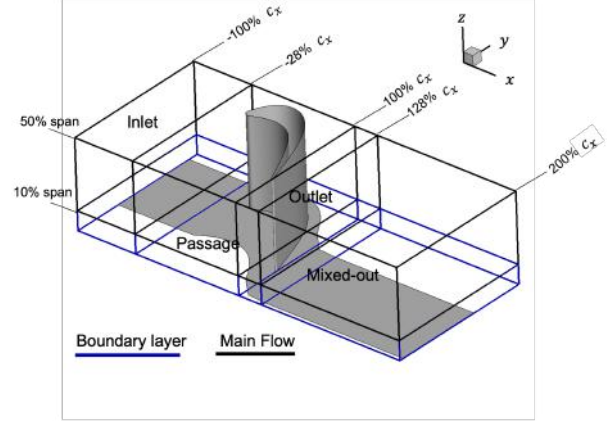


Figure 4 Mesh refinement zones in the computational domain. The blue lines shows the extent of the boundary layer cell refinement strategy to 10% span.

mesh sizes showed a constant difference of 0.004 WK^{-1} between \dot{S}_{genG} and \dot{S}_{genH} for each mesh case. For the case where a turbulent Transition SST model is used, \dot{S}_{gen} obtained using Equation 3 provided a closer match to $\Delta \dot{S}$ for any mesh size, so this method was selected in this paper. However, the trends of both \dot{S}_{genH} and \dot{S}_{genG} are the same, so the selection of either of them is not critical. Much of the variability in \dot{S}_{genG} and \dot{S}_{genH} in the SST model stems from the way the eddy viscosity is calculated (see [Martinez Castro \(2022\)](#)).

Figure 3 shows that at least a cell count of 30 million is needed to achieve a difference of less than 4% between \dot{S}_{gen} and $\Delta \dot{S}$. The value of $\Delta \dot{S}$ does not change significantly from the 5 million cells mesh, while the value of \dot{S}_{gen} over the full computational domain approaches the value of $\Delta \dot{S}$ when increasing the number of cells. Using the 5 million cells mesh, the difference between \dot{S}_{gen} and $\Delta \dot{S}$ was 9.8% and took 8 times less computing time. For this reason, using the 5 million cells mesh for the design optimisation was deemed as a good balance between computing time and level of entropy generation rate accuracy.

To study the loss distribution in the full computational domain, the ratio of entropy generation rate in each sub-domain to the total entropy generation rate in the full computational domain was calculated for the different regions in the domain and results are shown in Table 2. The inlet region for all mesh cases predicts the \dot{S}_{gen} by the inlet BL and this is 1% of the total entropy generation rate. The main difference comes in the Outlet region at the Main-Flow zone or Outlet-MF (see Figure 4) where there is a 4% higher \dot{S}_{gen} prediction with the 30 million cells mesh compared to the prediction that uses the 2.5 million cells mesh. This is the region where most of the secondary flow vortical structures are found. Significant differences can also be observed in the Passage-MF region where it was predicted a lower \dot{S}_{gen} with a higher number of cells. The difference in loss distribution between the 5 million cells mesh and the 30 million cells mesh in the Blade-Passage domain that includes the Passage-BL, Passage-MF, Outlet-BL and Outlet-MF is shown to be not larger than 2% in the Outlet-MF region and not larger than 1% for the other regions. This suggests that, as long as the mesh has enough cells in the BL region and an adequately fine grid in the secondary flow region, the use of a more spatially refined mesh for design is not justified.

Workflow of the PEW design optimisation based on minimum entropy generation rate

The PEW Design System is a computational tool developed at Durham University that uses Genetic Algorithms (GA) for PEW optimisation for the reduction of secondary loss. The whole process was iterated for 30 generations with a population of 100 each for a total of 3000 designs. More details about the PEW Design System can be found in [Martinez Castro \(2022\)](#). The cost function used to evaluate and select each design such that the features of the most successful ones are kept and improved in the design algorithm, was defined as:

$$cost = f_{w1}F_{sgen} + f_{w2}F_{yaw}, \quad (6)$$

where:

$$F_{sgen} = \frac{T_1 c_x}{\rho_1 U_1^3} \dot{S}_{gen}, \quad (7)$$

$$F_{yaw} = \begin{cases} 0, & \text{if } [\alpha_{mid} - \alpha] > 0 \\ |[\frac{\alpha_{mid} - \alpha}{\alpha_{mid}}]|, & \text{otherwise,} \end{cases} \quad (8)$$

and $f_{w1} = 15129.1343$ and $f_{w2} = 68.7$ are the weighting factors. This were defined to achieve a non-dimensional cost function with both terms having the same order of magnitude and making F_{sgen} the dominant term. The flow angle was

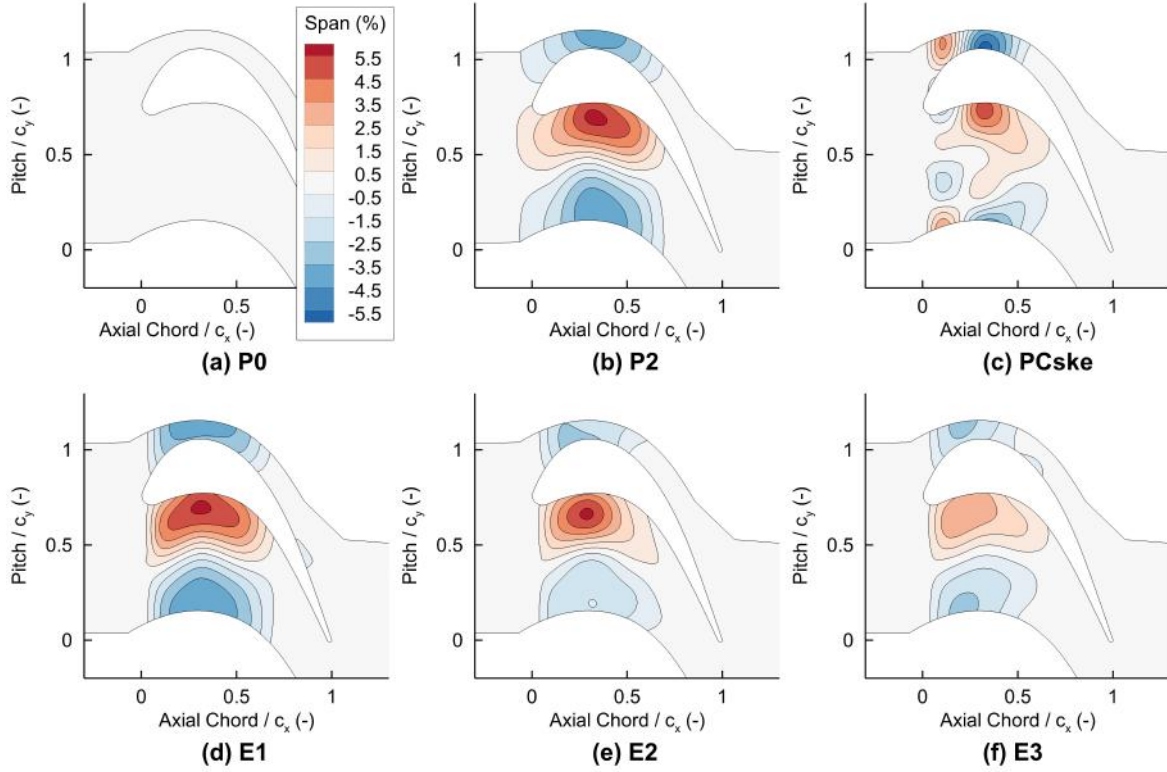


Figure 5 Profiled endwall geometries.

Table 3 Predicted cost function at 128% c_x

| | P0 | P2 | E1 | E2 | E3 | PC _{ske} |
|----------------------------------|--------|---------|---------|--------|--------|-------------------|
| $cost$ | 5.5553 | 5.1701 | 5.1203 | 5.0853 | 5.0761 | 9.5950 |
| $\dot{S}_{gen} (WK^{-1})$ | 0.0556 | 0.0517 | 0.0504 | 0.0502 | 0.0508 | 0.0960 |
| $\alpha - \alpha_{mid} (^\circ)$ | 0 | -0.0125 | -0.2223 | 0.1185 | 0.6526 | 0.0552 |
| $C_{ske} \times 10^{-4} (-)$ | 2.366 | 1.865 | 2.583 | 3.901 | 2.722 | 0.0175 |
| \dot{S}_{gen} improvement | 0% | 7.01% | 9.35% | 9.71% | 8.63% | -72.70% |

calculated at the 128% c_x plane using area-averaged values of velocity calculated via the CFD. The cost function penalised any reduction in flow turning relative to the midspan yaw angle value at the exit plane to avoid loss reduction by means of reducing the row loading. For an increase in flow turning relative to the midspan yaw angle value at exit, such as $F_{yaw} > 0$, the F_{yaw} component of the equation was set to 0. The PEW geometry was defined by 6 axial B-splines described by Fourier series defined by 5 variables each for a total of 30 design parameters. This changes the curvature of the endwall concavely and convexly (see [Martinez Castro \(2022\)](#)).

RESULTS AND DISCUSSION

Table 3 summarises the cost function value for the different geometries. The three designs with the lowest \dot{S}_{gen} after 30 generations were defined E1, E2 and E3, respectively and are shown in Figure 5. Two designs are shown for comparison, the "PC_{ske}" with the lowest C_{ske} but did not correspond with a reduction in \dot{S}_{gen} and the P2 reported to have the lowest C_{p0} of the P-series PEW for the Durham Cascade ([Gregory-Smith et al., 2001](#)). The E2 was selected for building and testing in the Durham Cascade because reported the lowest \dot{S}_{gen} of the optimised PEWs.

Numerical results

The cost function for the PEW is dependent on the \dot{S}_{gen} , so analysis of this variable through the passage is of relevance to find the loss sources and the \dot{S}_{gen} reduction mechanisms of PEW. To further investigate this, the contours of \dot{S}_{gen}''' were integrated in the radial direction up to 6% span, similar to [Denton and Pullan \(2012\)](#) and shown in Figure 6 as the entropy generation rate per unit surface area (\dot{S}_{gen}''). The integration up to 6% span made sure no vortical structures closer to the endwall, such as the HV nor the BL were missed out. The rest of the passage integrated in the radial direction from 6% to 50% span is shown in Figure 7. The profile loss is dominant above 6% span, so this is well captured in Figure 7.

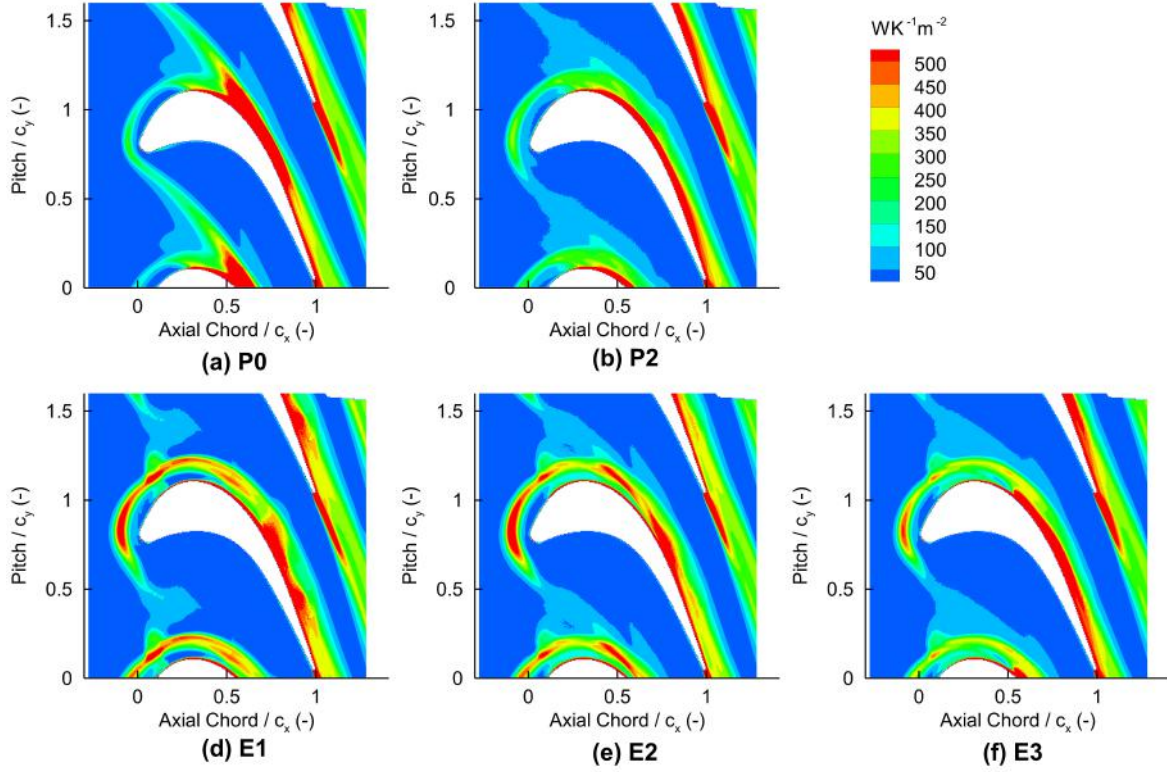


Figure 6 Entropy generation rate per unit surface area: Integral of \dot{S}_{gen}''' in the radial direction from 0% to 6% span.

Figure 6 shows that the P0 design features a cross-passage \dot{S}_{gen}'' region that mixes and increases over the SS of the pitchwise consecutive blade. This cross-passage \dot{S}_{gen}'' region is reduced in the spanwise direction in the PEW designs. A notable \dot{S}_{gen}'' region in the P0 is located on the blade SS approximately at $0.5 c_x$ near the endwall. This suggests the presence of a BL separation region which has been observed in earlier measurements in the Durham Cascade (Moore and Gregory-Smith, 1996). Notably, the LE region in E1, E2 and E3 has a higher \dot{S}_{gen}'' compared to P0. This evidence suggests a change in the formation of the HV.

After $0.5 c_x$ from the LE on the SS of the blade, the merging of the PSHV originated on the adjacent blade LE with the SSHV continues to take place in P0 in the streamwise direction until $0.825 c_x$ (see Figure 6). This is indicated by the large peak in the \dot{S}_{gen}'' in this region in P0. In the E-generation PEW, the \dot{S}_{gen}'' peaks cover a smaller area in the same region after $0.5 c_x$. In the case of E3 the \dot{S}_{gen}'' peak is located about $0.6 c_x$. This confirms a weakening of the interaction of the PSHV with the SSHV in the PEW delaying formation of the PV further downstream.

With the E3 PEW, there is less \dot{S}_{gen}'' compared to the E2 at the LE and suction surface. However, away from the endwall at about $0.28 c_x$ from the TE plane the E2 PEW shows a lower level of \dot{S}_{gen}'' (see Figure 7). Since the maximum level of \dot{S}_{gen}'' for E3 is concentrated in this region where most of the entropy generation occurs in the domain, it results in a larger \dot{S}_{gen} compared to E2. All cases with and without a PEW show that the most intense \dot{S}_{gen} region is the SS TE wake region (see Figure 7).

The static pressure field and the streamlines of the flow through the passage were plotted to investigate further the effect and origin of the PEW on the flow features that caused an \dot{S}_{gen} reduction. Figure 8 shows selected flow streamlines for the P0 a) and the E2 b) PEW traced bidirectionally from the 128% c_x main loss cores. The PSHV lines that are closer to the endwall in the E2 passage reduce the size of the PV when merging with the SSHV. This is due to the change in the radial pressure gradient derived from the geometrical "hump" shape of the E2 near the SS. The flow that produced the CV at the TE, was moved closer to the suction side of the blade, resulting in less main flow interaction with the CV. The E2 geometry produces a blockage at the LE that increases the intensity and thickness of the HSV. This produced higher \dot{S}_{gen}'' at the formation of the HSV.

To study the effect of the changes in vortex dynamics on the blade BL transition, the colour iso-levels of intermittency at 0.1 mm from the blade SS were plotted with axial plane contours of \dot{S}_{gen}''' , in Figure 9. The blue and dark blue (0 - 0.3) contours mean a fully laminar BL, the white and lighter blue (0.8 - 1.0) contours a fully turbulent BL and in between is a transitional BL. In both endwall geometries P0 and E2, the BL at the blade suction surface is mostly transitional, which explains why previous CFD simulations without transition turbulence models failed to predict loss accurately. Moreover, the blade SS BL transition starts after 50% c_x and does not complete until the TE. In the P0, the interaction of the SSHV with

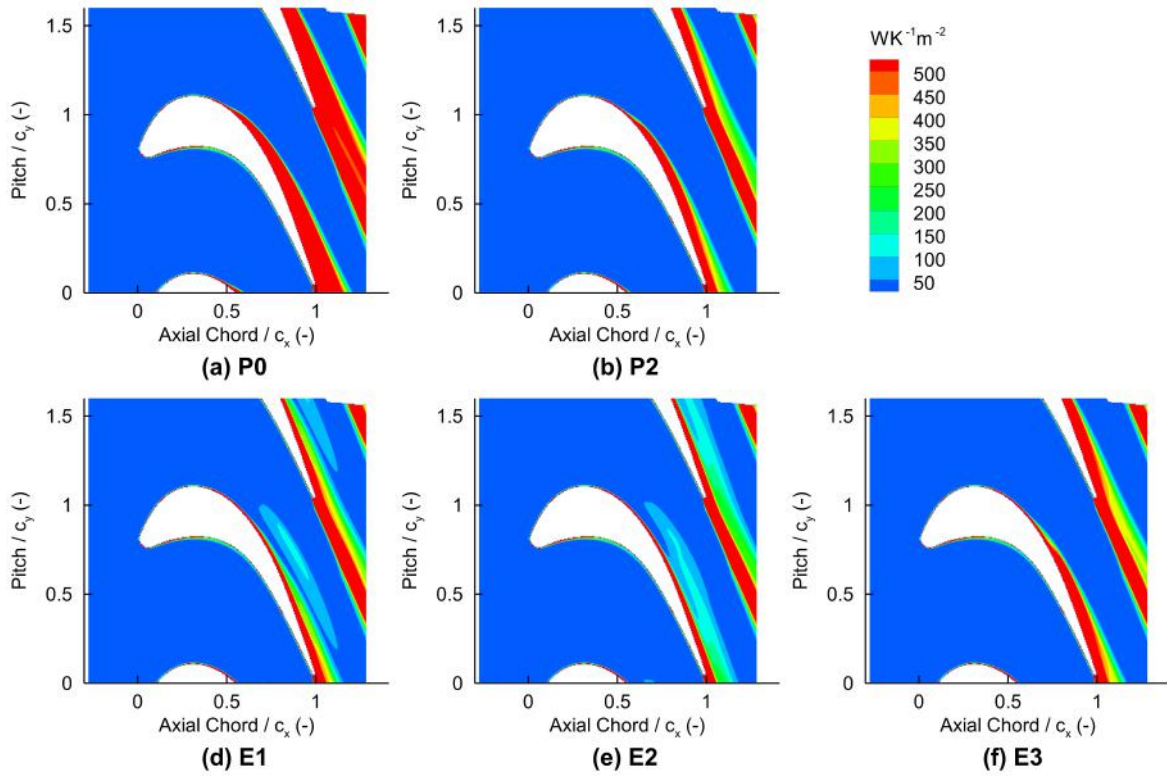


Figure 7 Entropy generation rate per unit surface area: Integral of \hat{S}_{gen}''' in the radial direction from 6% to 50% span.

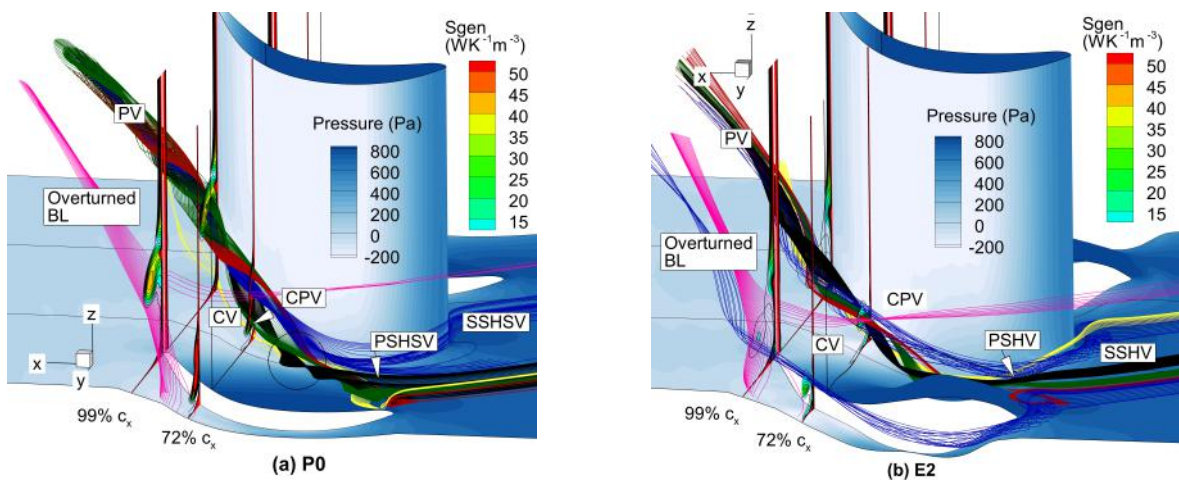


Figure 8 Secondary flow streamlines and \hat{S}_{gen}''' contours through the passage with static pressure contours for a) P0 and b) E2.

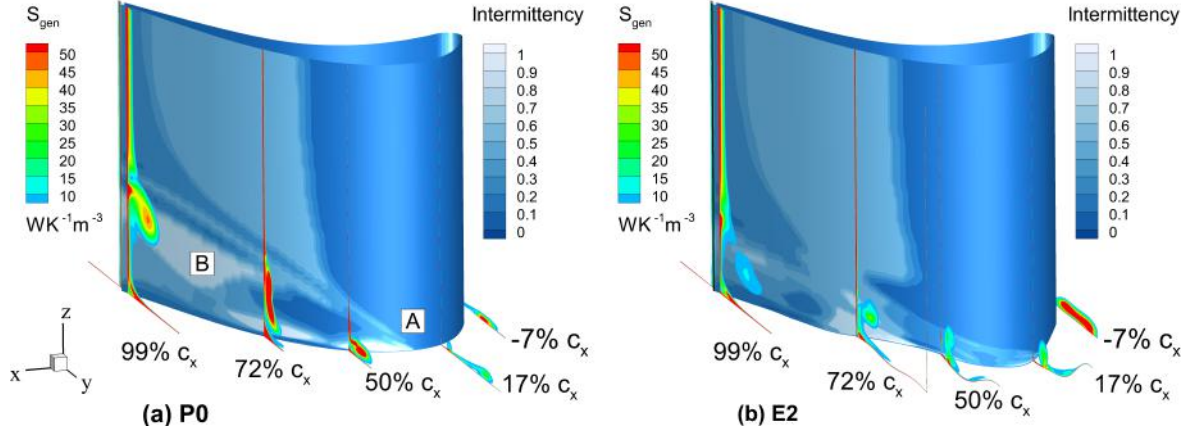


Figure 9 Intermittency contours at 0.1 mm from the blade surface and axial planes of entropy generation rate per unit volume for a) P0 and b) E2.

the cross-flow PSHV clearly shows a localised transition at the blade root upstream of the $0.5 c_x$ where indicated by black circle "A". This small region where the intermittency is 1.0, denoted by white in Figure 9 a), is followed by a blue area of low intermittency that stretches obliquely towards the passage midspan. The sudden change between an intermittency level of 1.0 to 0 is compatible with a local boundary layer BL flow measurements by Wang et al. (1997). The E2 in Figure 9 b) does not show an equivalent white region of turbulent BL upstream of $0.5 c_x$. A reason for this is that the effect of E2 of increasing the energy of the SSHV has avoided the separation of the flow at $50\% c_x$. The sequence of an intermittency region of value close to 1.0 followed by a large region of value close to 0 is present in both P0 and E2 around $72\% c_x$ close to the blade root in Figure 9 a). This large blade suction surface BL separation at the $72\% c_x$ plane is due to the merging of the cross-flow to the SSHV into the PSHV. The entropy generation rate produced by this feature is larger in P0, confirming that the weakening of the SSHV-PSHV interaction in the E2 reduces loss. As for the downstream region indicated by the black circle denoted "B" in Figure 9 a), shows that the P0 has a more likely turbulent blade SS BL, with a value of intermittency close to 1.0, and an increased BL separation zone from $72\% c_x$ that continues until the TE. The same region in the E2 PEW shows a value of intermittency between 0 and 1.0, which indicates a transitional BL less likely to be turbulent. This is related to the lower S''_{gen} observed in the E2 blade suction surface in Figure 7 indicated by the black circle.

Table 4 Area-averaged results at 128% c_x

| | Exp | | | CFD | | |
|----------|--------|--------|----------|--------|--------|----------|
| | P0 | E2 | Δ | P0 | E2 | Δ |
| C_{p0} | 0.2024 | 0.1783 | 0.0241 | 0.2318 | 0.2145 | 0.0173 |

Experimental Results

The experimental results confirm the predicted PV interaction mechanism and how is reduced by the effect of E2. For instance, at 75% axial chord plane (Figure 10), where the formation of the PV was shown, the effect of the E2 on the flow delays the formation of a larger PV loss core in the SS further downstream the passage. This is because the interaction of the PSHV with the SSHV has not taken place in the E2 as identified by the much weaker loss core in the near-wall region of 0.9 span. Due to the limitations on the probe size, it was not possible to measure further into the passage closer to the SS of the blade, so the SSHV for the E2 is not visible. However, the CFD predicted the SSHV in the E2 to be closer to the SS of the blade than in P0 (Figure 8). The E2 reduced the pitch-averaged C_{p0} , in particular between 0.8 to 0.85 span, where the P0 showed a three times a higher loss value (Figure 10 c). At the $128\% c_x$ traverse shown in Figure 11, the fully developed vortex system of the secondary flow is still recognisable in this axial plane before it mixes and dissipates further downstream. This plane provides a picture of the accumulated loss generated through the passage being carried downstream. The three main loss cores denoted as A, B, C are associated with vortical structure of the secondary flow. The largest reduction of loss was in the "B" loss core in E2. The single loss peak in E2 was a confirmation of the change in the secondary flow vortical structures far from the endwall. However, the major secondary flow vortex system formed by the PSHV and the SSHV in the E2 reduced its size and changed its location 0.05 of span closer to the endwall as a result of the weakening of the secondary flow observed from the $75\% c_x$ traverse. The area-averaged loss (Figure 11 c) showed a difference of midspan loss coefficient between E2 and P0 was 0.0028 which is deemed insignificant. So, the effect of the E2 on the midspan flow is negligible. The area-averaged results at the $128\% c_x$ are shown in Table 4. The agreement between the experimental and predicted results is deemed good.

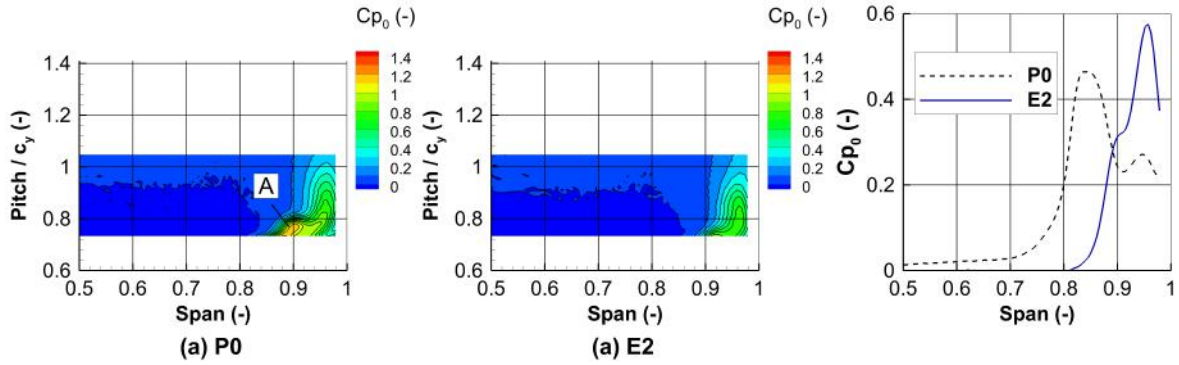


Figure 10 Experimental loss results for the 75% c_x ; a) P0 Cp_0 contour plots, b) E2 Cp_0 contour plots, c) Pitch-averaged Cp_0 . Span fraction normalised by the blade height.

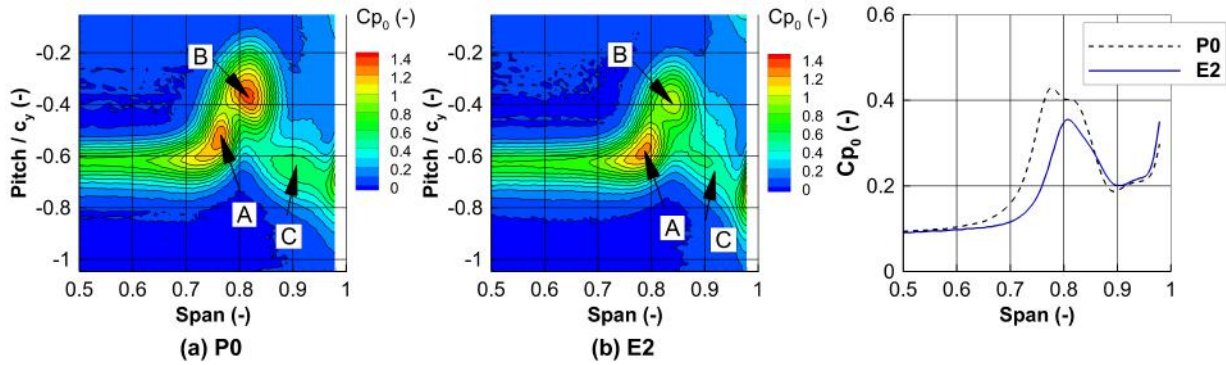


Figure 11 Experimental loss results for the 128% c_x ; a) P0 Cp_0 contour plots, b) E2 Cp_0 contour plots, c) Pitch-averaged Cp_0 .

Discussion

The results show that the E2 PEW delayed the formation of the largest loss core in the SS further down the passage. The location is consistent with the region where the PSHV meets the adjacent blade row SS. This is shown in Figure 7 as reduced area of the large loss cores in E2, associated to a less intense and closer to the wall PV shown in Figure 8 b). The analysis showed that the origin of this loss core can be traced to the formation of the PSHV that crosses the passage to the adjacent blade's suction surface. The effect of the PEWs in diminishing the cross-passage \dot{S}_{gen}'' region extent and in reducing the maximum value over the suction surface of the entropy generation rate region is responsible for the lower total entropy generation rate compared to P0. The cross-passage flow delayed the migration of the PSHV further downstream when the SSHV was more developed, resulting in a gradual interaction of the PV and the SSHV that merged into a single loss core. Figure 5 showed that this was caused by the higher pressure near the endwall on the SS as a result of the "dip" shape of the E2 geometry keeps the PV closer to the SS of the blade. This moved the corresponding loss core region closer to the endwall and in the tangential direction towards the blade SS compared to P0 and produced a more compact vortex structure closer to the endwall that effectively increases the 2D flow region in the radial direction.

The PEWs shapes that increased the intensity of the HV in particular the PSHV improved the overall performance of the blade passage. Particularly in E2, the "hump" in the LE increased the intensity of the HV which produced a large \dot{S}_{gen}'' but kept the PSHV closer to the wall (Figure 8) and as such changed the intensity of the PSHV cross-flow that interacts with the SSHV effectively reducing the shear stress between the PV and the counter-rotating SSHV keeping the vortical structures closer to the endwall and the suction surface.

This results confirmed the fundamental effect of the PEWs reported in the literature which is the weakening of the PV by changing the cross-passage pressure gradient. In addition the \dot{S}_{gen} analysis showed that the loss originates from the interaction of the PSHV with the SSHV. Notably, the intermittency analysis (Figure 9) showed that one effect to reduce entropy generation rate of the E2 PEW is also by reducing the BL transition and delay its separation on the blade SS.

The PEWs designs presented in this paper are optimised for the specific low-speed linear cascade. In a rotating cascade the unsteady effects of the passing blade and potential flow will introduce \dot{S}_{gen} by mixing and interacting with the secondary flow of the subsequent row (Jenny, 2012). If rotating effects and other conditions found in real turbine environments are considered, the minimisation of \dot{S}_{gen} as an objective function is expected to produce a better performing design as the \dot{S}_{gen} does not depend on the reference frame and is a direct measure of loss.

The measured results (Figures 10 and 11) showed a larger reduction in stagnation pressure loss which confirm the effec-

tiveness of the design system. The mesh resolution selected for the optimisation reported a 10% difference between ΔS and \dot{S}_{gen} . This uncertainty will be introduced in the correct estimation of \dot{S}_{gen} in the genetic algorithm. The experimental measurements showed that the numerical solution over-predicted the Cp_0 but the PEWs improvement ranking compared to P0 was kept. For this reason, is expected that a higher resolution mesh will increase the accuracy of the estimation of the real value of \dot{S}_{gen} in the algorithm and help it to converge faster but the design trend will not change considerably.

CONCLUSIONS

This paper employed entropy generation rate \dot{S}_{gen} as the primary optimisation design variable for a turbomachinery design problem. The PEW Design System used a Genetic Algorithm for automatic generation and evaluation of geometries and CFD to simulate the flow through a linear turbine cascade. The computational methods and calculations of entropy generation rate was explored, and a strategy was chosen. After 30 generations and evaluating a total of 3000 designs, an improved design was achieved. The successful design (E2) was manufactured, and experimental measurements validated the computational prediction by comparison with the baseline planar endwall (P0). The results were analysed to show the secondary loss reducing mechanisms associated with the use of PEWs in turbines. The key findings are:

- The method to calculate \dot{S}_{gen} depends on the turbulent model and mesh size to maintain an acceptable entropy generation rate balance. The method described by [Kock and Herwig \(2005\)](#) showed the best agreement between \dot{S}_{gen} and ΔS for the Transition SST $k - \omega$ turbulence model. A balance of 90% ΔS entropy generation rate was achieved with the 5 million cells mesh which was considered suitable for design optimisation purposes.
- The successful design (E2) predicted an improvement of 9.71% reduction in \dot{S}_{gen} and a 0.0173 reduction in Cp_0 compared to the flat endwall (P0).
- Profiled endwalls were found to reduce the secondary flow structures and so reducing the secondary loss of the cascade. This was achieved primarily by mitigating the migration of the pressure side horseshoe vortex and its interaction with the suction surface of the adjacent blade. Additionally, a reduction in boundary layer transition was identified due to a higher energy secondary separation horseshoe vortex. Therefore, a PEW design that weakens the formation of the horseshoe vortex and delays the point where the boundary layer becomes fully turbulent on the suction surface of the blade is desirable.

In summary, the study underscores the effectiveness of utilising entropy generation rate optimisation in improving PEW designs for turbomachinery, offering insights into loss reduction mechanisms and advocating for its broader application in aerodynamic design.

NOMENCLATURE

| | | | | | |
|--------------------|--------------------------------------|-------------------------------------|----------------|----------------------------------|--------------------------------------|
| C_{ske} | Secondary kinetic energy coefficient | [-] | α_{mid} | Yaw angle at midspan | [Degrees] |
| Cp_0 | Stagnation pressure loss coefficient | [-] | β | Empirical constant | [0.09] |
| c_x | Axial chord | [-] | Δs | Total change in specific entropy | [Jkg ⁻¹ K ⁻¹] |
| c_y | Pitch | [-] | μ | Dynamic viscosity | [Pas] |
| k | Specific turbulent kinetic energy | [m ² s ⁻²] | μ_t | Eddy viscosity | [Pas] |
| \dot{S}_{gen} | Entropy generation rate | [WK ⁻¹] | ρ | Density | [kgm ⁻³] |
| \dot{S}_{gen}''' | per unit volume | [WK ⁻¹ m ⁻³] | ω | Specific dissipation rate | [s ⁻¹] |
| \dot{S}_{gen}'' | per unit surface area | [WK ⁻¹ m ⁻²] | BL | Boundary layer | |
| U | Velocity magnitude | [ms ⁻¹] | CFD | Computational Fluid Dynamics | |
| U_{in} | Inlet velocity | [ms ⁻¹] | CV | Corner vortex | |
| U_{sec} | Secondary velocity | [ms ⁻¹] | HV | Horseshoe vortex | |
| u_z | Velocity component in z-direction | [ms ⁻¹] | LE | Leading edge | |
| T | Temperature | [K] | PEW | Profiled endwall | |
| x | Axial coordinate | [m] | PS | Pressure side | |
| y^+ | Non-dimensional wall distance | [-] | PV | Passage vortex | |
| y | Tangential coordinate | [m] | SS | Suction side | |
| α | Yaw angle | [Degrees] | TE | Trailing edge | |

ACKNOWLEDGMENTS

The authors gratefully acknowledge the support from Consejo Nacional de Ciencia y Tecnología, Mexico who financed Dr Martinez-Castro's PhD studies. The numerical and experimental data are available upon request.

REFERENCES

- Bergh, J., Snedden, G. and Dunn, D. (2020), 'Optimization of nonaxisymmetric endwall contours for the rotor of a low speed, 1 1/2-Stage research turbine with unshrouded blades—optimization and experimental validation', *Journal of Turbomachinery* **142**(4), 1–12.
- Brennan, G., Harvey, N. W., Rose, M. G., Fomison, N. and Taylor, M. D. (2001), Improving the efficiency of the Trent 500 HP turbine using non-axisymmetric end walls: Part 1 — Turbine design, in 'Proceedings of the ASME Turbo Expo 2001:V Power for Land, Sea, and Air. olume 1: Aircraft Engine; Marine; Turbomachinery; Microturbines and Small Turbomachinery', ASME, Louisiana.
URL: <http://proceedings.asmedigitalcollection.asme.org/proceeding.aspx?doi=10.1115/2001-GT-0444>
- Denton, J. D. (1993), 'The 1993 IGTI Scholar Lecture: Loss mechanisms in turbomachines', *ASME Journal of Turbomachinery* **115**(4), 621–656.
URL: <https://doi.org/10.1115/93-GT-435>
- Denton, J. and Pullan, G. (2012), A numerical investigation into the sources of endwall loss in axial flow turbines, in 'Proceedings of the ASME Turbo Expo 2012: Turbine Technical Conference and Exposition. Volume 8: Turbomachinery, Parts A, B, and C', Copenhagen, pp. 1417–1430.
URL: <http://proceedings.asmedigitalcollection.asme.org/proceeding.aspx?doi=10.1115/GT2012-69173>
- Gregory-Smith, D. G., Ingram, G., Jayaraman, P., Harvey, N. W. and Rose, M. G. (2001), 'Non-axisymmetric turbine end wall profiling', *Proceedings of the Institution of Mechanical Engineers, Part A: Journal of Power and Energy* **215**(6), 721–734.
- Grewe, R. P., Miller, R. J. and Hodson, H. P. (2014), The effect of endwall manufacturing variations on turbine performance, in 'Proceedings of the ASME Turbo Expo 2014: Turbine Technical Conference and Exposition. Volume 2C: Turbomachinery', Düsseldorf.
- Ingram, G. L. (2003), Endwall profiling for the reduction of secondary flow in turbines, PhD thesis, Durham University.
- Ingram, G. L., Gregory-Smith, D. G. and Harvey, N. W. (2005), 'Investigation of a novel secondary flow feature in a turbine cascade with end wall profiling', *ASME Journal of Turbomachinery* **127**(1), 209–214.
URL: <http://turbomachinery.asmedigitalcollection.asme.org/article.aspx?articleid=1466964>
- Jenny, P. (2012), Interaction Mechanisms Between Rim Seal Purge Flow and Profiled End Walls in a Low-Pressure Turbine, PhD thesis, Eidgenössische Technische Hochschule Zürich.
- Kadhim, H. T. and Rona, A. (2018), 'Design optimization workflow and performance analysis for contoured endwalls of axial turbines', *Energy* **149**, 875–889.
URL: <https://www.sciencedirect.com/science/article/pii/S0360544218302172>
- Kock, F. and Herwig, H. (2005), 'Entropy production calculation for turbulent shear flows and their implementation in cfd codes', *International Journal of Heat and Fluid Flow* **26**(4), 672–680.
URL: <https://doi.org/10.1016/j.ijheatfluidflow.2005.03.005>
- Li, H., Song, L., Li, Y. and Feng, Z. (2011), '2D Viscous aerodynamic shape design optimization for turbine blades based on adjoint method', *ASME Journal of Turbomachinery* **133**(3), 031014.
- Liu, H., Shen, X., Zhu, X., Du, Z., Yang, H. and Yang, R. (2017), The aerodynamic optimization design of turbine cascade with nonaxisymmetric endwall and experimental validations, in 'roceedings of the ASME Turbo Expo 2017: Turbomachinery Technical Conference and Exposition. Volume 2A: Turbomachinery', Charlotte.
- Martinez Castro, P. (2022), Entropy Generation Rate for Profiled Endwall Design in Turbines, PhD thesis, Durham University.
URL: <http://etheses.dur.ac.uk/14720/>
- Moore, H. and Gregory-Smith, D. G. (1996), Transition effects on secondary flows in a turbine cascade, in 'Proceedings of the ASME 1996 International Gas Turbine and Aeroengine Congress and Exhibition. Volume 1: Turbomachinery', ASME, Birmingham.
URL: <http://proceedings.asmedigitalcollection.asme.org/proceeding.aspx?doi=10.1115/96-GT-100>
- Przytarski, P. J. and Wheeler, A. P. S. (2021), 'Accurate prediction of loss using high fidelity methods', *ASME Journal of Turbomachinery* **143**(3), 031008.

- Rose, M. G. (1994), Non-axisymmetric endwall profiling in the HP NGV's of an axial flow gas turbine, *in* 'Proceedings of the ASME 1994 International Gas Turbine and Aeroengine Congress and Exposition. Volume 1: Turbomachinery', ASME, The Hague.
URL: <http://proceedings.asmedigitalcollection.asme.org/proceeding.aspx?doi=10.1115/94-GT-249>
- Shahpar, S., Caloni, S. and de Prieëlle, L. (2017), 'Automatic Design Optimization of Profiled Endwalls Including Real Geometrical Effects to Minimize Turbine Secondary Flows', *Journal of Turbomachinery* **139**(7).
URL: <https://asmedigitalcollection.asme.org/turbomachinery/article/doi/10.1115/1.4035510/378860/Automatic-Design-Optimization-of-Profiled-Endwalls>
- Sieverding, C. H. (1985), 'Recent progress in the understanding of basic aspects of secondary flows in turbine blade passages', *ASME Journal of Engineering for Gas Turbines and Power* **107**(2), 248–257.
URL: <http://gasturbinespower.asmedigitalcollection.asme.org/article.aspx?articleid=1416074>
- Wang, D. X., He, L., Li, Y. S. and Wells, R. G. (2010), 'Adjoint aerodynamic design optimization for blades in multistage turbomachines-Part II: Validation and application', *ASME Journal of Turbomachinery* **132**(2), 021012.
- Wang, H. P., Olson, S. J., Goldstein, R. J. and Eckert, E. R. G. (1997), 'Flow visualization in a linear turbine cascade of high performance turbine blades', *ASME Journal of Turbomachinery* **119**(1), 1–8.
URL: <http://turbomachinery.asmedigitalcollection.asme.org/article.aspx?articleid=1465125>
- Whittle, F. (1981), *Gas Turbine Aero-Thermodynamics*, Pergamon.
- Zlatinov, M. B., Tan, C. S., Montgomery, M., Islam, T. and Seco-Soley, M. (2011), Turbine hub and shroud sealing flow loss mechanisms, *in* 'Proceedings of the ASME 2011 Turbo Expo: Turbine Technical Conference and Exposition. Volume 7: Turbomachinery, Parts A, B, and C', ASME, Vancouver, pp. 947–959.
URL: <http://proceedings.asmedigitalcollection.asme.org/proceeding.aspx?articleid=1633882>